Available online at www.sciencedirect.com
ScienceDirect
Trans. Nonferrous Met. Soc. China 29(2019) 213−221
Transactions of Nonferrous Metals Society of China
www.tnmsc.cn

Cold model on bubble growth and detachment in bottom blowing process

Hong-jie YAN[1,2], Jun-bing XIAO[1,2], Yan-po SONG[1,2], Zhi-wen HU[1,2], Zhi-kai TAN[1,2], Liu LIU[1,2]

1. School of Energy Science and Engineering, Central South University, Changsha 410083, China;
2. Hunan Key Laboratory of Energy Conservation in Process Industry,
Central South University, Changsha 410083, China

Received 26 February 2018; accepted 7 September 2018

Abstract: The bubble growth and detachment behavior in the bottom blowing process were investigated. Four multi-hole nozzle configurations with different opening ratios were assessed experimentally using high-speed photography and digital image processing. For these configurations, the experiments reveal that the bubble growth consists of a petal-like stage, an expansion stage and a detachment stage. The petal-like shape is qualitatively described through the captured images, while the non-spherical bubbles are analyzed by the aspect ratio. The bubble size at the detachment is quantified by the maximum caliper distance and the bubble equivalent diameter. Considering the dependence on the opening ratio, different prediction models for the ratio of maximum caliper distance to hydraulic diameter of the nozzle outlet and the dimensionless bubble diameter are established. The comparative analysis results show that the proposed prediction model can accurately predict the bubble detachment size under the condition of multi-hole nozzles.

Key words: bottom blowing; bubble growth; nozzle geometry; non-spherical bubble

1 Introduction

Recently, bottom blowing furnace is employed in many industrial processes, such as copper smelting process [1,2], lead-smelting process [3] and steelmaking process [4,5]. The advantages of high smelting efficiency, low capital cost, low energy consumption and reduced dust generation result in broad application of this technique in the industry [6−8]. In copper smelting process, oxygen enriched air is injected into the furnace through lances with gear-like geometry [6], which can stir up the liquid and participate in the complicated gas−liquid reactions. The injected gas not only causes nozzle erosion but also damages the refractory bricks [6,9], thereby deteriorating the performance and lifetime of the reactors. However, the geometry of the lance is rarely investigated, though it is one of the most important components in gas injection assembly. Using dimensional analysis, KRISHNAPISHARODY and IRONS [10] concluded that the characteristics of the generated gas−liquid plume are independent of the type of nozzle. In their work, the hydraulic characteristics of the gas injection were discussed and studied by a modified Froude number $Fr_m=\rho_g\cdot Q^2/\rho_l\cdot g\cdot d_o^5$ [10], where ρ_g is the gas density, ρ_l is the liquid density, g is acceleration due to gravity, Q is the gas flow rate and d_o is the inner nozzle diameter. However, if a nozzle is similar to the gear-like geometry, it is reasonable to use the hydraulic diameter of nozzle in the modified Froude number. Therefore, the hydraulic characteristics of the gas injection are influenced by the geometry of the lance or nozzle.

In the bottom blowing process, bubble formation at the nozzle outlet is important for determining the initial bubble shape and size in the gas−liquid system. The bubble shape is mainly controlled by the upward and restraining forces acting on the forming bubble, which are primarily related to the physical properties of fluid, bubble size, bubble velocity, etc [11,12]. According to the shape of generated bubble, spherical and non-spherical models were developed for categorizing different bubble formation processes [13]. For the spherical models, a two-stage approach including

Foundation item: Project (51676211) supported by the National Natural Science Foundation of China; Project (2015zzts044) supported by Innovation Foundation for Postgraduate of Central South University, China; Project (2017SK2253) supported by the Key R&D Plan of Hunan Province, China

Corresponding author: Liu LIU; Tel: +86-731-88830239; E-mail: l.liu@csu.edu.cn

DOI: 10.1016/S1003-6326(18)64930-1

expansion stage and detachment stage was proposed by WRAITH [14], which assumed that the bubble detached with a radius same as the orifice radius. Additionally, a three-stage model was developed with an intermediate waiting stage by using potential flow theory. In this approach, no outflow of gas from the orifice for a short time after the detachment was assumed [13]. YANG et al [15] categorized bubble formation into three stages namely expansion stage, elongation stage and pinch-off stage. In the category of the non-spherical models, a theoretical method was proposed by interfacial element approach [16]. In their work, the effect of necking of the bubble surface was considered. However, most of these formation models were formulated based on the investigations on circular nozzle or orifice, while the multi-hole nozzles are frequently used in actual situation. The study of the shape evolution during bubble formation process from a multi-hole nozzle configuration is really in high demand. Usually, the aspect ratio of the bubble is used to describe its shape, which is defined as the ratio of minor to major axis of the bubble, i.e., the ratio of its height to its width [11,12]. Therefore, the relationship between the bubble shape and the aspect ratio was investigated in this work.

The size of the submerged gas bubble is mainly affected by the gas flow through the orifice, the shape and dimension of orifice, etc. KUMAR and KULOOR [17] proposed a correlation for predicting the bubble volume using orifice gas flow rate and gravitational acceleration. The study of DAVIDSON and SCHÜLER [18] reported that the bubble size at the detachment depends on shape and dimension of the orifice. For the multi-hole configuration, JIANG and CHENG [19] concluded that the number of holes of multi-hole orifices affects the bubble size. In our previous work [20], a prediction model for bubble detachment diameter was developed using the multi-hole nozzles with different circular holes. This model included the effects of the nozzle opening ratio, the inner diameter, and Reynolds number. However, the bubble size for the gear-like multi-hole nozzle configuration is with high significance but has not been studied so far, which is the prime objective of this work.

A simple model for bubble formation was proposed by GADDIS and VOGELPOHL [21]. The model considers the expansion stage and detachment stage during the bubble formation process. Simple bubble geometry with the forces acting on it is shown in Fig. 1. The buoyancy force F_B, pressure force F_P, and force due to gas momentum F_M are the upward forces. While, surface tension force F_S, drag force F_D and inertia force F_I are the restraining forces. The prediction of the bubble detachment diameter was developed considering bubble diameter, nozzle diameter, bubble velocity, etc. In the expansion stage, the bubble remains attached to the nozzle exit until the resultant lifting forces just exceed the resultant restraining forces. It was assumed that the detachment stage starts right after the occurrence of force imbalance. Meanwhile, a gas neck connecting the bubble to the nozzle exists during all stages. Finally, the bubble detaches from the nozzle when this gas neck contracts. To simplify the bubble growth from the multi-hole nozzle configurations, the description of bubble growth from a single hole was used in this work.

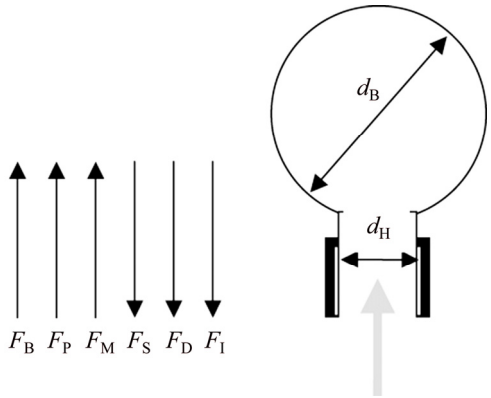

Fig. 1 Spherical bubble attached to nozzle through a cylindrical neck [21]

The present work was conducted to investigate the bubble growth and detachment behavior in the bottom blowing process. Four multi-hole nozzle configurations with different opening ratios were used collaborating with high-speed photography and digital image processing. The bubble shape was qualitatively described through the captured images, while the non-spherical bubbles were analyzed by the aspect ratio. The bubble size at the detachment was quantified by the maximum caliper distance and the bubble equivalent diameter. In addition, the influence of the gas flow rate and the opening ratio on the bubble shape and detachment diameter was accessed.

2 Experimental

2.1 Experimental setup

Figure 2 presents the schematic diagram of the experimental setup for investigation on the bubble growth and detachment behavior by simplifying the cold model experimental setup in our previous work [22]. The transparent liquid container was made of acrylic glass, with the dimensions of 150 mm × 150 mm × 500 mm, opening at the top to atmosphere. Treated tap water was filled into the liquid container up to a liquid height of 360 mm from the nozzle exit. The nozzle configurations were fixed at the bottom of the container.

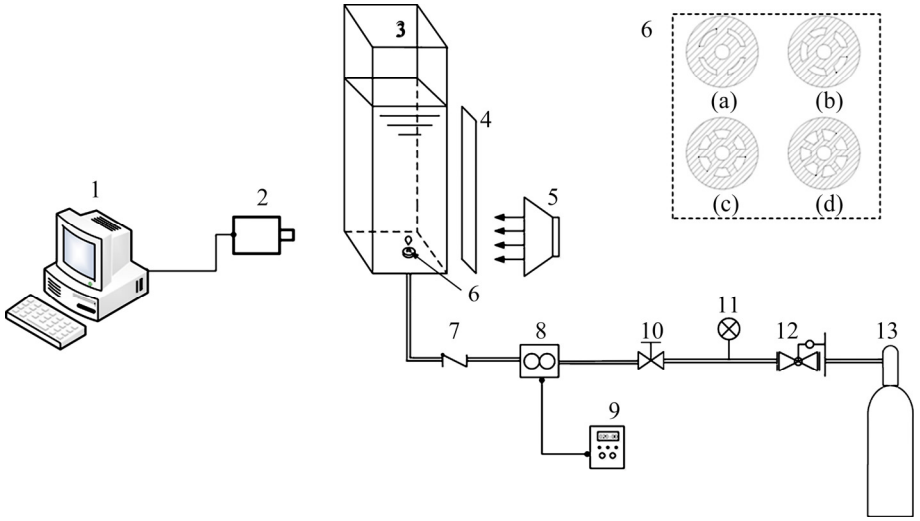

Fig. 2 Schematic diagram of experimental setup: 1−Computer; 2−High speed camera; 3−Vessel; 4−Diffuse; 5−LED lamp; 6−Multi-hole nozzle; 7−Check valve; 8−Mass flowmeter; 9−Digital display; 10−Valve; 11−Manometer; 12−Pressure reducing valve; 13−Gas cylinder

A pressure reducing valve was utilized to minimize the fluctuation of gas flow at the outlet of gas cylinder. Prior to measurement, the gas was charged until its pressure became constant. The gas flow rate Q in the pipe was metered by a digital mass flowmeter with a range of 0−200 L/min. To avoid water entering into the gas pipeline, a check valve was placed between the nozzle and the mass flowmeter. All experiments were performed at a reference temperature of 25 °C and a pressure of 101.325 Pa. A ruler was placed at the front wall of the vessel as a scale label for the high-speed camera. A filter paper was installed at the vessel wall for distributing light uniformly over the test section. The images of the bubble growth and detachment were recorded by a high-speed video system (FASTCAM SA1.1 200K, Photron Co., Japan) with a LED lamp as the light source. Prior to recording, the gas was released into the liquid for 10 s to stabilize the bubble growth and detachment. The temporal resolution was set at 1000 fps, and at least 1500 frames were captured.

The in-house nozzle configurations were manufactured by fixing the internal diameter of the central and varying the diameter of the surrounding holes. In the view of the industrial gear-like nozzle configuration [6], four nozzle configurations, i.e., 5-hole nozzle (Fig. 2(a)), 6-hole nozzle (Fig. 2(b)), 7-hole nozzle (Fig. 2(c)) and 8-hole nozzle (Fig. 2(d)) were used. For these configurations, the external nozzle diameter was 12 mm and the ratio of the length of the holes to the total length of the nozzles was kept constant as 1:4.

The opening ratio ε was introduced, which was defined as the total area of the holes divided by the inner flow area of nozzle in front of the holes. Mathematically, it can be written as

$$\varepsilon = \sum_{i=1}^{n} A_{oi} \Big/ A_N \tag{1}$$

where A_N is the internal area of the nozzle. For simplifying the complicated release of the gas through the multi-hole nozzles, the surrounding holes were regarded as round holes, and the hydraulic diameter of the surrounding holes was used in this work. The main parameters of the nozzles are presented in Table 1, including diameter of the central hole D_c, hydraulic diameter of the surrounding hole D_s, sum of the areas of the holes $\sum_{i=1}^{n} A_{oi}$, hydraulic diameter of the nozzle outlet D_o, and opening ratio of the corresponding nozzle configurations.

Table 1 Parameters of corresponding nozzle configurations

ε	$D_c/10^{-3}$ m	$D_s/10^{-3}$ m	$\sum_{i=1}^{n} A_{oi}$ /10^{-6} m^2	$D_o/10^{-3}$ m
0.34	2.5	1.309	17.090	1.551
0.41	2.5	1.575	20.609	1.828
0.47	2.5	1.718	23.625	1.873
0.53	2.5	1.737	26.641	1.875

The gas flow rate Q used at the inlet of nozzle configurations was within the range of $(1-4)\times10^{-4}$ m^3/s. Afterwards, the gas flow rate Q_o at the outlet of nozzle configurations can be obtained by conservation of mass. The flow through the orifice is proportional to its cross-sectional area, hence, Q_o is calculated as

$$Q_o = Q/\varepsilon \tag{2}$$

The gas flow rates Q and Q_o at the inlet and outlet of nozzle configurations are given in Table 2.

Table 2 Gas flow rates at outlet of nozzle configurations

$Q/(10^{-4}\ m^3\cdot s^{-1})$	$Q_o/(10^{-4}\ m^3\cdot s^{-1})$			
	ε=0.34	ε=0.41	ε=0.47	ε=0.53
1	2.94	2.44	2.13	1.89
1.5	4.41	3.66	3.19	2.83
2	5.88	4.88	4.26	3.77
2.5	7.35	6.10	5.32	4.72
3	8.82	7.32	6.38	5.66
3.5	1.03	8.54	7.45	6.60
4	1.18	9.76	8.51	7.55

2.2 Measurement method

The captured images were processed as follows.

(1) The images of bubbles at the detachment were selected and subtracted by the initial background images.

(2) The images obtained from previous step were converted to binary images for the detection of bubble boundaries.

(3) The bubble area A_b, aspect ratio E and maximum caliper distance L_d [23] were thereafter measured.

(4) These steps were performed using open source image processing program ImageJ. The parameters mentioned in (3) were calculated by averaging the measurement from at least five series of separated bubbles.

The bubble equivalent diameter d_B at detachment is calculated as

$$d_B = \sqrt{\frac{4A_b}{\pi}} \tag{3}$$

In addition, the dimensionless bubble diameter d^* was introduced, by scaling d_B with the hydraulic diameter of the nozzle outlet as

$$d^* = d_B/d_H \tag{4}$$

Here, hydraulic diameter of the nozzle outlet d_H was obtained as

$$d_H = \frac{4\sum_{i=1}^{n} A_{oi}}{\sum_{i=1}^{n} P_{oi}} \tag{5}$$

where A_{oi}, P_{oi} and n are the cross-sectional area of each hole, perimeter of each hole, and the number of individual holes, respectively.

The maximum caliper distance was introduced for measuring the bubble size, which is the longest distance between any two points along the bubble boundary. The ratio of maximum caliper distance to hydraulic diameter of the nozzle outlet L_d^* was defined as

$$L_d^* = L_d/d_H \tag{6}$$

3 Results and discussion

3.1 Bubble shape

3.1.1 Description of bubble shape

Bubbles with petal-like shape under conditions of low gas flow rates were observed in the present experiments, which showed different behaviors compared with the existing literatures [10,18]. The typical images for ε=0.34 and Q_o=2.94×10^{-4} m^3/s are presented in Fig. 3, where the spines on the bubble surface are red marked. The first image represents 200 ms after the start of gas injection and subsequent images are shown at 4 ms intervals. At the very beginning of the bubble growth, the lifting forces are lower than the restraining forces. This leads to the horizontal expansion shown in Fig. 3(a). The gas released from the holes rapidly coalesces into a bubble body because the separating distance between the holes is insufficient to obstruct gas to coalescence. Afterwards, the vertical expansion dominates the bubble growth. Due to the gas from the center faces less drag force than that from the surrounding holes, the center part of bubble moves faster than the surroundings leading to the appearance of the tip bulge. Meanwhile, the gas from surrounding holes plays a role of pulling the bubble and slowing the bubble rising. Subsequently, the interaction between the gases from different holes results in the appearance of the petal-like shape. This special shape in the bubble growth is mainly due to the influence of the nozzle geometry.

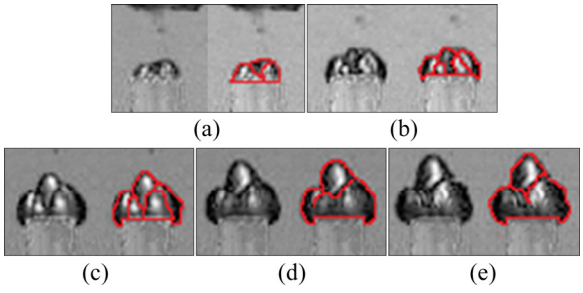

Fig. 3 Images of bubble growth in petal-like shape: (a) 200 ms; (b) 204 ms; (c) 208 ms; (d) 212 ms; (e) 214 ms

With the increase of the bubble volume, a smooth bubble surface without distinct spine is attained after the petal-like period is terminated (see Fig. 4(e)). After a gradual expansion, the bubble begins to lift up with a small gas neck connected to the nozzle exit (see Fig. 4(f)). This indicates the start of the bubble detachment. Eventually, the bubble detaches from the

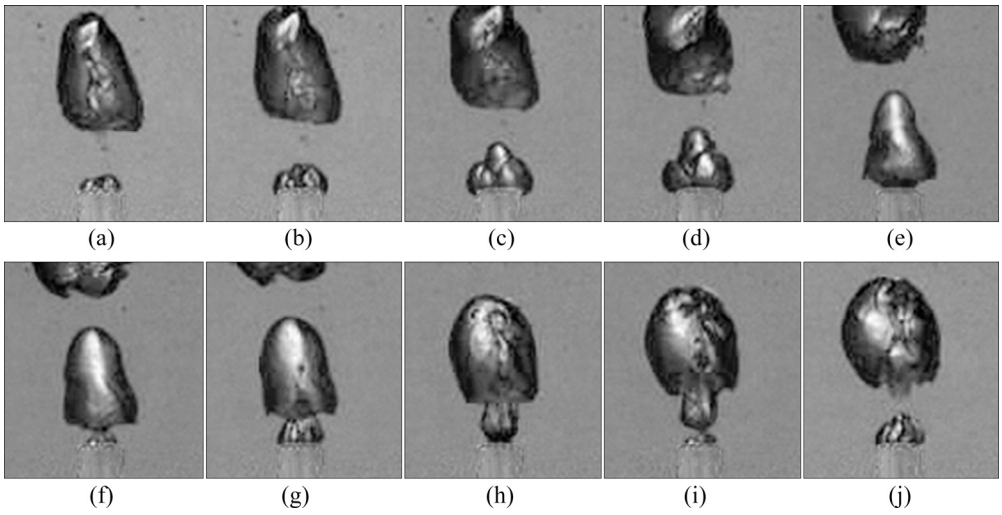

Fig. 4 Images of bubble formation under conditions of ε=0.34 and Q_o=2.94×10^{-4} m^3/s: (a) 200 ms; (b) 204 ms; (c) 210 ms; (d) 216 ms; (e) 230 ms; (f) 240 ms; (g) 246 ms; (h) 258 ms; (i) 264 ms; (j) 270 ms

nozzle after the gas neck contracts (see Fig. 4(j)). It should be noted that the bubble has a non-spherical shape during the whole process.

In general, the bubble growth process under a multi-hole nozzle configuration can be characterized by a non-spherical model, which consists of three stages, namely petal-like stage, expansion stage and detachment stage. Compared to previous studies, the present work proposes an additional stage when bubbles are of petal-like shape. This work explains the qualitative characteristics of the petal-like shape, though its characteristics are not quantified here.

3.1.2 Aspect ratio

The bubble aspect ratio at the detachment is plotted in Fig. 5 for describing the bubble shape. For constant opening ratio, the relationship between bubble aspect ratio and diameter is not clear. The reason for such phenomenon could be explained by the existence of the contracted gas neck at detachment. It has been widely accepted that a bubble is of a spherical shape when the aspect ratio equals unity [8−10]. Based on the range of aspect ratio in this work (1.107−1.490), it can be concluded that the bubble shape at detachment is non-spherical. Referring to the earlier stated description of bubble shape, the center part of bubble rises faster than the surrounding, resulting in the phenomenon that the height of bubble is larger than its width, and eventually, aspect ratio is larger than unity.

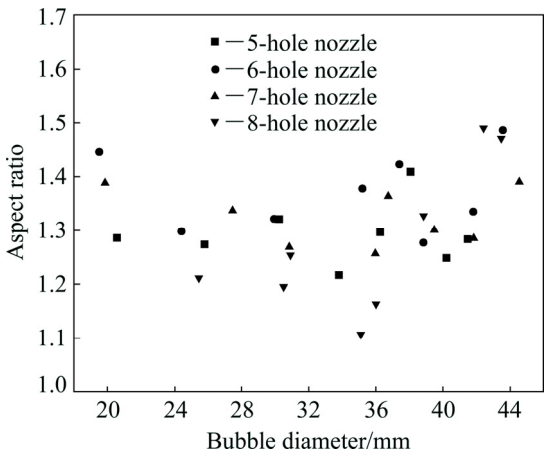

Fig. 5 Plots of bubble aspect ratio versus bubble diameter

3.2 Bubble size

3.2.1 Bubble equivalent diameter

Figure 6(a) shows the variation of the bubble equivalent diameter at detachment under different experimental conditions. The bubble diameters are in a range of 24.4−46.6 mm, which are mostly more than twice of the nozzle outside diameter. This indicates that the WRAITH's [14] assumption is not adapted to the situations with bubbles generated from the multi-hole nozzle. It can be seen that the bubble diameter at opening ratio ε=0.47 is close to that at opening ratio ε=0.53. This indicates that the influence of the opening ratio on bubble size can be equal when the opening ratios are large. However, there is obvious difference between the results from opening ratios ε=0.34 and ε=0.41. Clearly, the bubble diameter increases with the increase of the volumetric gas flow under a constant opening ratio. From Fig. 6(b), the bubble diameters increase initially and then decrease with increasing opening ratio in most cases. This indicates the influence of opening ratios on the bubble diameter has a limitation. However, for the cases of 1.0×10^{-4} and 1.5×10^{-4} m^3/s, the bubble diameters decrease initially and then increase with increasing opening ratio at low flow rate. This could be due to the

instability of bubble generation at low flow rates. Therefore, the bubble size depends on the gas flow rate and opening ratios.

According to the existing literatures [12−16] and the aforementioned analysis, the bubble size is a function of the size and shape of the orifice, gas flow rate and so forth. Based on the previous correlation of bubble diameter and the experimental results, a new predictive model for the dimensionless bubble diameter is presented including the opening ratio ε:

$$d^* = k_1 \cdot \varepsilon^{a_1} \cdot \left(\frac{Q_o^{0.4}}{g^{0.2} d_H} \right)^{b_1} \tag{7}$$

where k_1, a_1 and b_1 are undetermined coefficients.

Based on regression analysis, the undetermined coefficients are obtained. The new predictive model is proposed as

$$d^* = 2.554\varepsilon^{0.412} \cdot \left(\frac{Q_o^{0.4}}{g^{0.2} d_H} \right)^{0.847} \tag{8}$$

Substituting Eq. (6) to Eq. (8), there is

$$d^* = 2.554\varepsilon^{0.06} \cdot \left(\frac{Q^{0.4}}{g^{0.2} d_H} \right)^{0.847} \tag{9}$$

The exponent of the opening ratio is very small, indicating that the influence of the opening ratio can be ignored. A fitting of the data with a coefficient of determination of R^2=0.95 is performed. Consequently, the dimensionless bubble diameter can be expressed as

$$d^* = 2.574 \left(\frac{Q^{0.4}}{g^{0.2} d_H} \right)^{0.820} \tag{10}$$

The results show that the proposed model can predict the bubble detachment diameter with reasonable accuracy under given experimental conditions.

In the literatures [12,16−19,21], bubble diameter has been mostly expressed as a function of gas flow rate, acceleration due to gravity, nozzle diameter, liquid density and so on. A comparison of the models from KUMAR and KULOOR [17] and GADDIS and VOGELPOHL [21] with the present model (see Table 3) was carried out based on the experimental conditions, as shown in Fig. 7.

For Model 1, the predicted diameter is greater than the experimental data under opening ratio ε=0.34 and ε=0.41. However, it is close to the experimental data when opening ratio is ε=0. 47 and ε=0.53. This indicates that Model 1 is inappropriate for predicting bubble diameter under the multi-hole nozzle configuration. As for Model 2, a reasonable prediction can be achieved under the condition that the opening ratio is quite small (ε=0.34). However, the predictions deviate from experimental data gradually with the increase of the opening ratio. The prediction with Model 3 is consistent with the experiment data very well. MAPE, Std. Dev. and R^2 of different models are given in Table 4.

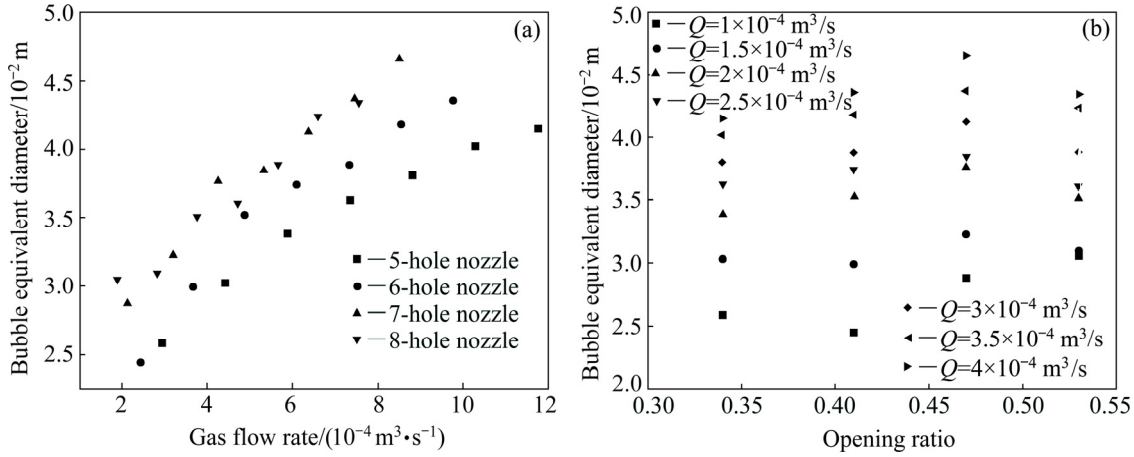

Fig. 6 Effects of gas flow rate (a) and opening ratio (b) on bubble equivalent diameter

Table 3 Typical prediction models for bubble diameter

Model	Correlation	Source	D_o/mm
1	$d^* = \left(\frac{5.856}{\pi} \cdot \frac{Q_o^{1.2}}{g^{0.6}} \right)^{1/3} / d_H$	Ref. [17]	1.1−3
2	$d^* = [\left(\frac{6D_o\sigma_{LG}}{\rho_L g} \right)^{4/3} + \left(\frac{81\nu Q_o}{\pi g} \right) + \left(\frac{135Q_o^2}{4\pi^2 g} \right)^{4/5}]^{1/4} / d_H$	Ref. [21]	0.2−6
3	$d^* = 2.574 \left(\frac{Q^{0.4}}{g^{0.2} d_H} \right)^{0.820}$	Present work	1.56−1.88

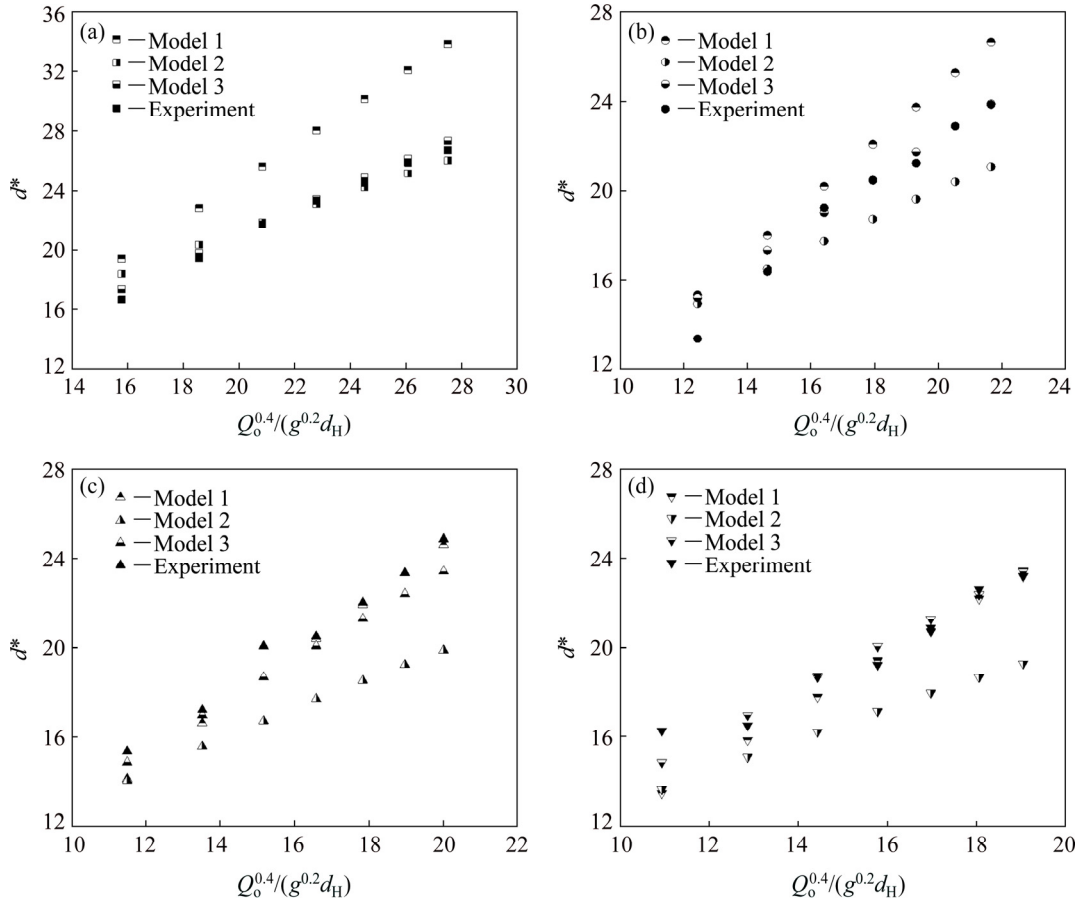

Fig. 7 Comparative analysis for different models: (a) ε=0.34; (b) ε=0.41; (c) ε=0.47; (d) ε=0.53

Table 4 Indicators of models in replicating present experimental results

Model	MAPE/%	Std. Dev.	R^2
1	0.095	2.846	−
2	0.079	2.130	0.595
3	0.029	0.744	0.953

Therefore, it is concluded that the proposed prediction model performs well for predicting the bubble diameter.

3.2.2 Maximum caliper distance

The bubble maximum caliper distance is presented in Fig. 8. For a constant opening ratio, the maximum caliper distance shows an increasing trend with the gas flow rate increasing. This indicates that the bubble size becomes larger with increasing gas flow rate. Here, the ratio of the maximum caliper distance to hydraulic diameter of the nozzle outlet L_d^* is used to study the bubble size. Similar to the analysis of bubble equivalent diameter, a predictive model of L_d^* is developed considering gas flow rate at the nozzle outlet, the opening ratio and hydraulic diameter of the nozzle outlet:

$$L_d^* = k \cdot \varepsilon^a \cdot \left(\frac{Q^{0.4}}{g^{0.2} d_H} \right)^b \tag{11}$$

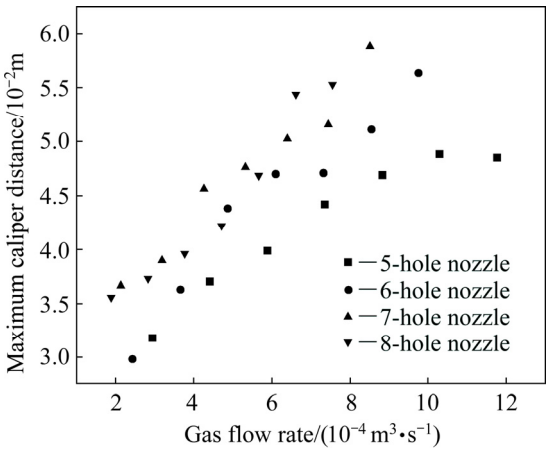

Fig. 8 Effect of gas flow rate on bubble maximum caliper distance

where k, a and b are undetermined coefficients. Consequently, by applying the least square method, Eq. (11) can be then expressed as

$$L_d^* = 2.992\varepsilon^{0.099} \cdot \left(\frac{Q^{0.4}}{g^{0.2} d_H} \right)^{0.872} \tag{12}$$

The coefficient of determination R^2 is 0.924. The comparison of the predictive data with the experimental

data is shown in Fig. 9. It can be concluded that, the opening ratio should be taken into account in the study of bubble size for multi-hole nozzle configuration regarding bubble maximum caliper distance. This is consistent with the conclusion in the analysis of bubble equivalent diameter.

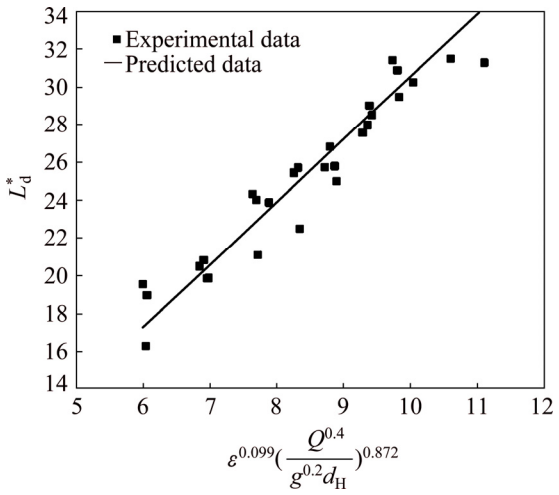

Fig. 9 Comparison of predicted data with experimental data

4 Conclusions

(1) The bubble growth from a multi-hole nozzle can be classified using a non-spherical model with three stages, namely petal-like stage, expansion stage and detachment stage.

(2) The petal-like shape is described qualitatively through the captured images and the non-spherical shape is analyzed by the aspect ratio.

(3) The maximum caliper distance and the bubble equivalent diameter are applied to analyzing the bubble size at the detachment.

(4) Following the dependence of the opening ratio, different predictive models for the ratio of the maximum caliper distance to hydraulic diameter of the nozzle outlet and dimensionless bubble diameter are proposed. These proposed models can give precise prediction for the bubble size.

Acknowledgments

One of the authors (Jun-bing XIAO) gratefully acknowledges the financial support from China Scholarship Council. The authors also wish to thank Mr. Vineet VISHWAKARMA for his valuable comments on this work.

References

[1] WANG Qing-meng, GUO Xue-yi, TIAN Qing-hua. Copper smelting mechanism in oxygen bottom-blown furnace [J]. Transactions of Nonferrous Metals Society of China, 2017, 27(4): 946−953.

[2] WANG Qing-meng, GUO Xue-yi, WANG Song-song, LIAO Li-le, TIAN Qing-hua. Multiphase equilibrium modeling of oxygen bottom-blown copper smelting process [J]. Transactions of Nonferrous Metals Society of China, 2017, 27(11): 2503−2511.

[3] BAI Lu, XIE Ming-hui, ZHANG Yue, QIAO Qi. Pollution prevention and control measures for the bottom blowing furnace of a lead-smelting process, based on a mathematical model and simulation [J]. Journal of Cleaner Production, 2017, 159: 432−445.

[4] WEI Guang-sheng, ZHU Rong, DONG Kai, MA Guo-hong, CHENG Ting. Research and analysis on the physical and chemical properties of molten bath with bottom-blowing in EAF steelmaking process [J]. Metallurgical and Materials Transactions B, 2016, 47(5): 3066−3079.

[5] LIU L, KEPLINGER O, MA T, ZIEGENHEIN T, SHEVCHENKO N, ECKERT S, YAN H, LUCAS D. Euler-Euler simulation and X-ray measurement of bubble chain in a shallow container filled with liquid metals [J]. Chemical Engineering Science, 2018, 192: 288−305.

[6] COURSOL P, MACKEY P J, KAPUSTA J P, VALENCIA N C. Energy consumption in copper smelting: A new Asian horse in the race [J]. JOM, 2015, 67(5):1066−1074.

[7] SHUI L, CUI Z, MA X, RHAMDHANI MA, NGUYEN A, ZHAO B. Mixing phenomena in a bottom blown copper smelter: A water model study [J]. Metallurgical and Materials Transactions B, 2015, 46(3): 1218−1225.

[8] WEI G, ZHU R, DONG K, LI Z, YANG L, WU X. Influence of bottom-blowing gas species on the nitrogen content in molten steel during the EAF steelmaking process [J]. Ironmaking & Steelmaking, 2017, 21: 1−8.

[9] YANG Q, BJÖRKMAN B, CARLSSON G. Effects of bubble expansion on wear of refractory for BOF stirring plugs embedding tuyeres [J]. Steel Research International, 1997, 68(3): 107−114.

[10] KRISHNAPISHARODY K, IRONS G A. A critical review of the modified Froude number in ladle metallurgy [J]. Metallurgical and Materials Transactions B, 2013, 44(6): 1486−1498.

[11] LIU L, YAN H, ZHAO G. Experimental studies on the shape and motion of air bubbles in viscous liquids [J]. Experimental Thermal and Fluid Science, 2015, 62: 109−121.

[12] LIU L, YAN H, ZHAO G, ZHUANG J. Experimental studies on the terminal velocity of air bubbles in water and glycerol aqueous solution [J]. Experimental Thermal and Fluid Science, 2016, 78: 254−265.

[13] KULKARNI A A, JOSHI J B. Bubble formation and bubble rise velocity in gas-liquid systems: A review [J]. Industrial & Engineering Chemistry Research, 2005, 44(16): 5873−5931.

[14] WRAITH A E. Two stage bubble growth at a submerged plate orifice [J]. Chemical Engineering Science, 1971, 26(10): 1659−1671.

[15] YANG L, DIETRICH N, LOUBIÈRE K, GOURDON C, HÉBRARD G. Visualization and characterization of gas–liquid mass transfer around a Taylor bubble right after the formation stage in microreactors [J]. Chemical Engineering Science, 2016, 143: 364−368.

[16] XIAO Z, TAN R B. An improved model for bubble formation using the boundary-integral method [J]. Chemical Engineering Science, 2005, 60(1): 179−186.

[17] KUMAR R, KULOOR N K. The formation of bubbles and drops [J]. Advances in Chemical Engineering, 1970, 8: 255−368.

[18] DAVIDSON J F, SCHÜLER B O G. Bubble formation at an orifice in a viscous liquid [J]. Chemical Engineering Research and Design, 1997, 75: S105−S115.

[19] JIANG F, CHENG G G. Effects of gas injection with multihole orifices in upleg snorkel on bubble behaviour and decarburisation rate during RH refining [J]. Ironmaking & Steelmaking, 2012, 39(5): 386−390.

[20] YAN H, XIAO J, HU Z. Experimental investigation on bubble formation from multi-hole nozzles [C]//Sustainable Industrial

Processing Summit SIPS 2016. Canada: FLOGEN Star Outreach, 2016: 199−212.
[21] GADDIS E S, VOGELPOHL A. Bubble formation in quiescent liquids under constant flow conditions [J]. Chemical Engineering Science, 1986, 41(1): 97−105.
[22] YAN H J, LIU F K, ZHANG Z Y, GAO Q, LIU L, CUI Z X, SHEN D B. Influence of lance arrangement on bottom-blowing bath smelting process [J]. The Chinese Journal of Nonferrous Metals, 2012, 22: 2393−2400. (in Chinese)
[23] MERKUS H G. Particle size measurements: Fundamentals, practice, quality [M]. The Netherlands: Springer Science & Business Media, 2009.

底吹过程中气泡生长和脱落的冷态模型

闫红杰[1,2]，肖俊兵[1,2]，宋彦坡[1,2]，胡志文[1,2]，谭智凯[1,2]，刘 柳[1,2]

1. 中南大学 能源科学与工程学院，长沙 410083；
2. 中南大学 流程工业节能湖南省重点实验室，长沙 410083

摘 要：结合高速摄影和数字图像处理技术，采用 4 种不同开口率的多孔喷嘴结构研究底吹过程中气泡的生长和脱离行为。实验结果表明，多孔喷嘴结构条件下的气泡生长过程由花瓣状阶段、膨胀阶段和分离阶段组成。通过实验获得的气泡图像对花瓣状气泡进行定性描述，并且通过纵横比定量分析非球形气泡形状变化规律。此外，采用最大卡尺距离和气泡当量直径分析气泡脱离尺寸。通过考虑气泡脱离直径与开口率的关系，分别建立基于最大卡尺距离与喷嘴出口水力直径比的无量纲气泡直径的预测模型。对比分析结果表明，提出的预测模型能够准确预测多孔喷嘴结构条件下的气泡脱离尺寸。

关键词：底吹；气泡生长；喷嘴几何形状；非球形气泡

(Edited by Bing YANG)